Influence of skin depth on convective heat transfer in induction heating.

Sébastien Renaudière de Vaux, Rémi Zamansky, Wladimir Bergez, Philippe Tordjeman, Viviane Bouyer, Jean-François Haquet

INFLUENCE OF SKIN DEPTH ON CONVECTIVE HEAT TRANSFER IN INDUCTION HEATING

S. Renaudière de Vaux[1,2], *R. Zamansky*[2], *W. Bergez*[2], *Ph. Tordjeman*[2], *V. Bouyer*[1], *J.-F. Haquet*[1]

[1] *CEA, DEN, Cadarache, SMTA/LPMA, F13108 St Paul lez Durance, France*
[2] *Institut de Mécanique des Fluides de Toulouse (IMFT), Université de Toulouse, CNRS-INPT-UPS, Toulouse, France*

We investigate convection driven by induction heating of a horizontal fluid layer using direct numerical simulations (DNS). This problem is of particular interest in the context of nuclear severe accident mastering. In a real severe accident, the molten core is subjected to homogeneous internal sources resulting from nuclear disintegrations. This situation is mimicked in the laboratory using induction heating as the internal source. In induction heating, however, heat sources are localized in the skin layer. Consequently, this concentration of heat may modify the flow and wall heat transfer compared to the case of homogeneous internal sources. DNS are carried out for three typical skin depths and three total deposited powers. Skin depth variations show surprising results regarding flow structures and heat transfer. It is found that the heat sources' heterogeneity has a weak effect on flow patterns. Consequently, models of heat transfer in the case of homogeneous sources remain valid even with strong localized heating near the bottom.

Introduction. Magnetic fields, whether AC or DC, are used in industry for numerous purposes, such as electromagnetic stirring, induction heating or metal casting [1, 2]. Natural convection in the presence of DC magnetic fields has received a lot of attention thanks to geophysical applications among others [3, 4]. The case of AC magnetic fields and induction heating is less studied, although it is of common use in the area of nuclear safety research in the context of severe accidents [5]. In the case of a nuclear core meltdown, the molten core (called corium) interacts with the concrete containment structures. This phenomenon is not yet fully understood. A key issue is the prediction of the convective wall heat transfer, since the ablation rate of the concrete is proportional to it [5]. The molten corium-concrete interaction (MCCI) is studied in the CEA Severe Accident Laboratory to predict the ablation rate. To model the volumetric heat generation due to nuclear disintegrations, AC magnetic fields are used, as Joule dissipation mimics the volumetric power generation. In a real severe accident, the source term is more or less homogeneous. The relevance of MCCI tests relies on the low influence of the skin depth which, in this case, is around 1/3 of the pool size, on the wall heat transfer. The effects of the source term concentration in the skin layer have to be analyzed. But heat transfer and fluid structure studies in experimental devices are complicated due to high temperature opacity, multiphase flow, etc. As a model, we solve using DNS a horizontal fluid layer of thickness h of an electrically conducting fluid subjected to a horizontal AC magnetic field $B_0 \cos \omega t \, \mathbf{e}_x$, as shown in Fig. 1, with B_0 being the imposed magnetic field amplitude at the bottom boundary and ω the pulsation.

This case shares similarities with Rayleigh-Bénard convection (RBC), although there is no imposed temperature difference. Diffusion of the magnetic field $\mathbf{B}$ in the layer generates eddy currents $\mathbf{j} = j(z)\mathbf{e}_y$ over a characteristic length scale called the skin depth $\delta = \sqrt{2\eta/\omega}$, with $\eta = 1/\mu_0\sigma$ being the magnetic diffusion coefficient, and a Joule heat source term j^2/σ, with σ being the fluid electrical

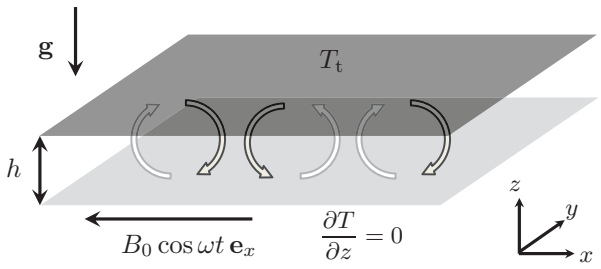

Fig. 1. Sketch of the studied configuration.

conductivity and σ the vacuum permeability. Moreover, the Lorentz force is purely irrotational, $\mathbf{F}_\mathrm{L} = \mathbf{j} \times \mathbf{B} = F_\mathrm{L}(z)\mathbf{e}_z$, as the layer is infinitely horizontally wide. This configuration is representative of a homogeneous region of the flow, where $(\mathbf{B} \cdot \nabla)\mathbf{B} = 0$. Near the edges, $(\mathbf{B} \cdot \nabla)\mathbf{B} \neq 0$ and there would be a stirring effect of the Lorentz force. Therefore, the destabilization of the layer is only due to the temperature gradients, and this case is similar to the convection driven by internal sources concentrated in the skin layer. When $\delta/h \leq 0.5$, the Joule term is exponentially decaying from the bottom. The deposited power is given by the Rayleigh number $\mathrm{Ra} = g\beta\Delta T h^3/\nu\kappa$. Here, $\mathbf{g} = -g\,\mathbf{e_z}$ is the gravitational acceleration, β is the fluid thermal expansion coefficient, ν is the fluid kinematic viscosity, κ is the heat diffusivity and ΔT is a reference temperature proportional to the deposited power defined in section 1. Similarly to RBC, the onset of the instability is characterized by a critical Rayleigh number $\mathrm{Ra_c}(\delta/h)$. Linear stability analysis has been used to show that reducing δ/h promotes the destabilization of the layer, the critical Rayleigh number is slightly reduced [6]. Natural convection with homogeneous internal sources has been widely studied [7]. Recently, Goluskin and van der Poel [8] studied with DNS the case of uniform sources. Their results highlight non-symmetrical velocity profiles at sufficiently large Ra. In the case of AC magnetic field induced convection, the concentration of heat in the skin layer is susceptible to fundamentally rework the flow. This could question the interpretation of MCCI tests. We investigate with DNS this problem for three characteristic skin depths, $\delta/h = 0.45$, 0.14 and 0.04 and for three total deposited powers. In section 1, we describe the studied problem and our numerical tools. In section 2, we analyze and comment our results regarding heat transfer and fluid structures.

1. Physical and numerical modelling. We consider small magnetic Reynolds number flows in an infinitely wide cavity in the (x, y)-directions. The nondimensional electromagnetic field is governed by

$$\frac{\partial \mathbf{B}}{\partial t} = \frac{\mathrm{Pr}}{\mathrm{Pm}} \triangle \mathbf{B}, \quad \mathbf{j} = \frac{h}{\delta} \nabla \times \mathbf{B}, \tag{1}$$

$$\mathbf{B} = \cos\omega t, \quad \text{at } z = 0, \tag{2}$$

$$\mathbf{B} = 0, \quad \text{at } z = 1. \tag{3}$$

To nondimensionalize the length, time, magnetic field and current density, h, $t_0 = h^2/\kappa$, B_0 and $j_0 = B_0/\mu_0\delta$ are used. Here, $\mathrm{Pr} = \nu/\kappa$, $\mathrm{Pm} = \nu/\eta$ are the thermal and magnetic Prandtl numbers, ω is a non-dimensional pulsation. These equations are solved analytically, using a series expansion. Furthermore, we assume that the magnetohydrostatic hypothesis is valid: the period of the magnetic field is much smaller than all other relevant hydrodynamic timescales [1].

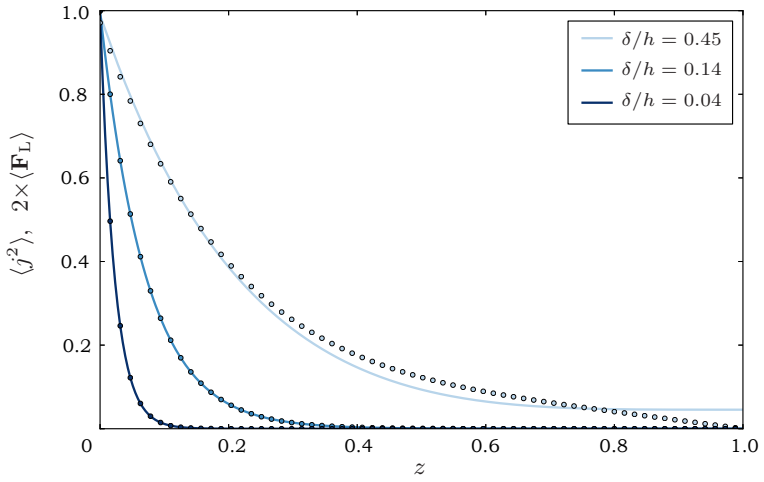

Fig. 2. Lorentz force (circles) and Joule term (solid lines) profiles for the computed points.

This given, the Lorentz force and Joule effect can be averaged over a period of magnetic field:

$$\langle F_\mathrm{L}\rangle \mathbf{e}_z = \frac{1}{\tau_\omega}\int_t^{t+\tau_\omega} \mathbf{j}\times\mathbf{B}\,\mathrm{d}t', \quad \text{and} \quad \langle j^2\rangle = \frac{1}{\tau_\omega}\int_t^{t+\tau_\omega} \mathbf{j}^2\mathrm{d}t' \tag{4}$$

with $\tau_\omega = 2\pi/\omega$. These terms are exponentially decaying in the $\delta/h \ll 1$ limit, as seen in Fig. 2. This given, the total space–time power deposited in the volume is

$$\Gamma = \int_0^1 \langle j^2\rangle \mathrm{d}z \approx \frac{\delta}{2h}\left[1-\exp\left(-\frac{2h}{\delta}\right)\right].$$

The Lorentz force in Eqs. (4) can be rewritten as the gradient of the pressure term $\langle F_\mathrm{L}\rangle\mathbf{e_z} = -\delta/h\nabla\langle\mathbf{B}^2\rangle/2$. The studied configuration in Fig. 1 is governed by the non-dimensional Navier–Stokes equations, continuity equation, heat equation and boundary conditions

$$\frac{\partial \mathbf{u}}{\partial t} + (\mathbf{u}\cdot\nabla)\mathbf{u} = -\nabla p^\star + \mathrm{Pr}\,\triangle\mathbf{u} + \mathrm{Ra}\ \mathrm{Pr}\,T\mathbf{e_z}, \tag{5}$$

$$\nabla\cdot\mathbf{u} = 0, \tag{6}$$

$$\frac{\partial T}{\partial t} + (\mathbf{u}\cdot\nabla)T = \triangle T + \frac{1}{\Gamma}\langle j^2\rangle, \tag{7}$$

$$\mathbf{u} = 0, \quad \frac{\partial T}{\partial z} = 0 \quad \text{at } z = 0, \tag{8}$$

$$\mathbf{u} = 0, \quad T = 0 \quad \text{at } z = 1. \tag{9}$$

Here $\mathbf{u} = (U, V, W)$, T are, respectively, the dimensionless velocity and temperature. The velocity scale is h/t_0. The modified pressure $p^\star$ is the pressure supplemented by the magnetic pressure, in units of $\rho(\kappa/h)^2$. The magnetic pressure is $Ha^2\,\mathrm{Pr}\,/\mathrm{Pm}\langle\mathbf{B}^2\rangle/2$, with $Ha = B_0 h\sqrt{\sigma/\rho\nu}$ being the Hartmann number. As it has only a pressure component, the Lorentz force has no effect here. The boundary conditions (8) and (9) correspond to an insulating medium on the bottom and to

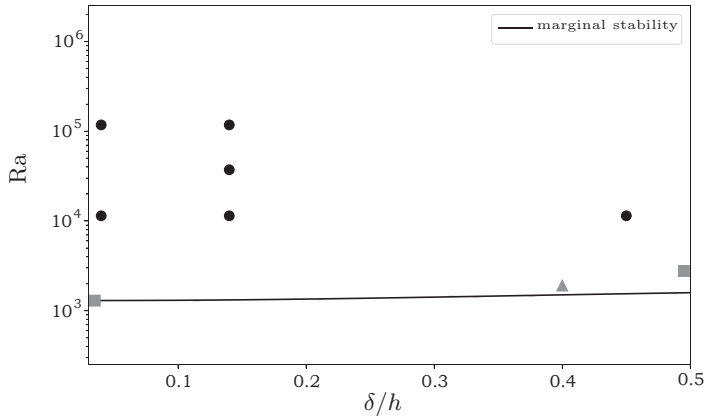

Fig. 3. Computed points in the parameter space (circles). The black line is the marginal stability computed by linear stability analysis. The gray squares indicate Ra_c in the limits $\delta/h = 0$ and $\delta/h \to \infty$. The gray triangle is Ra_c from [6].

a perfect conductor on the top. The reference temperature used to nondimensionalize the equations is built as

$$\Delta T = \frac{\Gamma h^2 j_0^2}{\rho c_p \kappa \sigma} \tag{10}$$

similarly to [7]. This definition is based on the power deposited in the whole layer regardless of the localization (i.e. regardless of δ/h). With this definition, Ra is characteristic of the total deposited power. We solve Eqs. (5) to (9) using the finite volume code Jadim [9] in a square box of horizontal aspect ratio 10 and periodic boundary conditions in horizontal directions. The code is based on a third order Runge–Kutta scheme for temporal advancement and a semi-implicit Crank–Nicolson shceme for diffusive terms. The numerical mesh is consituted of $N_x \times N_y \times N_z = 512 \times 512 \times 128$ regularly spaced cells. The mesh convergence was checked, there was less than 1% difference between the temperature and velocity profiles and the integrated quantities (i.e. root mean square velocity and mean temperature). The time step δ_t is dictated by the CFL condition $\max(|\mathbf{u}|)\delta_t/\delta_x = 1$, with δ_x being the space step. In our DNS, this corresponds to $\delta_t/\tau_\kappa \simeq 5 \times 10^{-6}$. The Lorentz force and Joule profiles from Eqs. (4) and Fig. 2 are prescribed in the DNS. To emphasize liquid metals, the values of the Prandtl numbers are fixed, $\mathrm{Pr} = 0.025$ and $\mathrm{Pm} = 1.55 \times 10^{-6}$. The computed points are given in Fig. 3, with the marginal stability (black line) on an indicative basis. With this set of points, it is possible to clarify the relative influence of Ra and δ/h.

2. Simulation results.

2.1. Fluid structures. After a transient regime, the flow reaches a stationary regime which we describe here. Instantaneous snapshots of the z-component of the velocity are shown in Fig. 4 for $\mathrm{Ra} = 1.14 \times 10^4$.

The flow structures are qualitatively identical, regardless of the skin depth. Contrary to the DC magnetic field convection, the flow exhibits a spectrum of wavelengths and not a single observed wavelength [4]. The dominant wavenumber defined in Fig. 1 is around $k \approx 2.5$ for all cases, as it is the case in RBC [4]. Moreover, one notices that they share the same color scale. This means that for the same Ra, the characteristic kinetic energy $\overline{W^2}$ is the same (the bar denotes

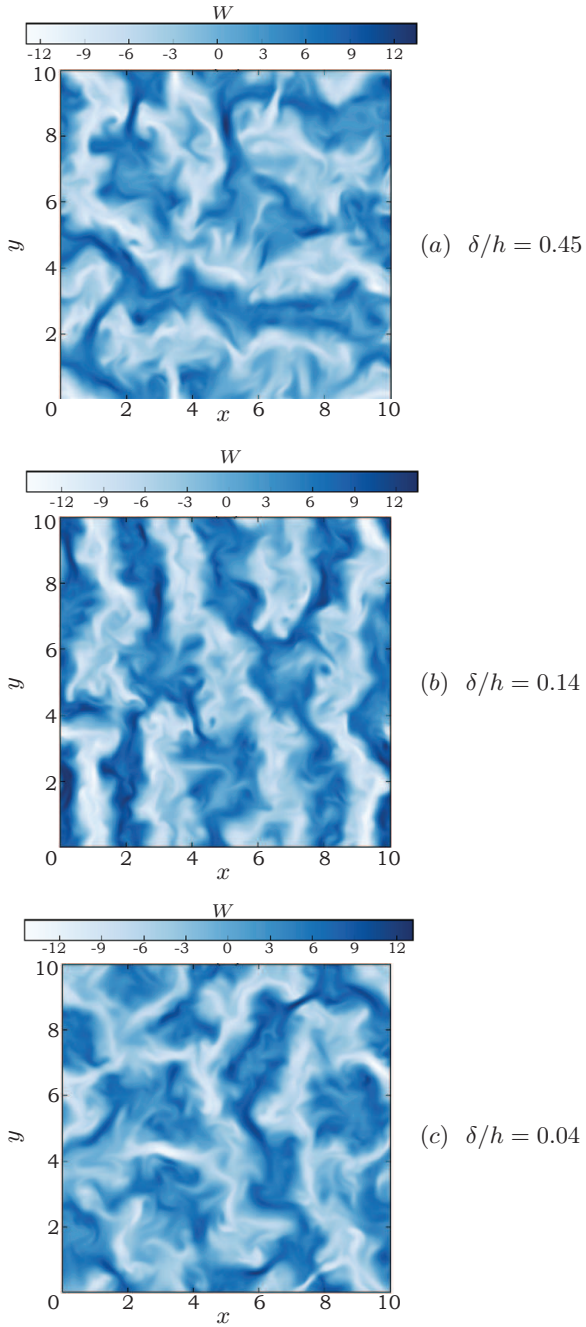

Fig. 4. Snapshots of the vertical component of velocity at (*a*) $\delta/h = 0.45$, (*b*) $\delta/h = 0.14$, and (*c*) $\delta/h = 0.04$.

averaging in horizontal directions). It is balanced by the energy input given by Ra. Therefore, one expects that

$$\overline{W^2} \sim \mathrm{Ra}. \tag{11}$$

This scaling is verified in DNS, where we find $\overline{W^2} \sim \mathrm{Ra}^{1.02}$, which shows the poor

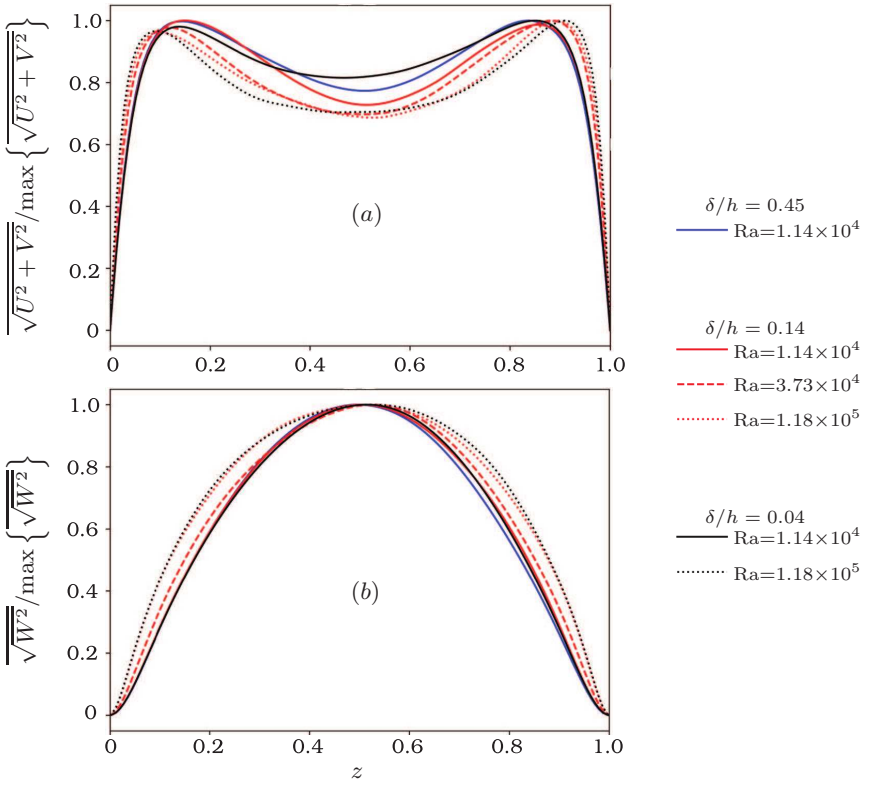

Fig. 5. Vertical profiles of (a) the horizontal velocity component and (b) vertical velocity component.

influence of δ/h on the kinetic energy. Furthermore, the skin depth has a weak influence on the horizontal and vertical velocity profiles, as seen in Fig. 5a and Fig. 5b, respectively.

The profiles are averaged in time and the bar denotes averaging in the horizontal directions. In Fig. 5a, one can see that the boundary layer thickness (defined as the distance between the wall and the maximum velocity) does not depend on δ/h: the curves at the same Ra are superimposed in the boundary layer. However, as expected, it decreases as Ra increases. The same conclusions are drawn for the vertical velocity profiles. The influence of δ/h on the velocity profiles is weak. The maximum of $\sqrt{\overline{W^2}}$ is located at $z = 1/2$. The increase in preferential heating towards the bottom does not displace the maximum of $\sqrt{\overline{W^2}}$. On the opposite, an increase in Ra spreads the $\sqrt{\overline{W^2}}$ profiles. The skin depth has a low influence on the convective structures. However, the preferential heating may modify the temperature profiles and, hence, the heat transfer.

2.2. Heat transfer. Fig. 6 gives the average temperature profiles. A loss of symmetry can be noted compared to the Rayleigh-Bénard case.

This is due to the combined effect of the insulating condition (8) and of the non-symmetrical volume heating. The temperature difference between the top and the bottom is dictated by Ra. When Ra increases, the bottom wall temperature decreases due to the convective motion, which eases the heat evacuation through the top. For $\delta/h < 0.45$, all temperature profiles display an inflection point for $0.1 \leq z \leq 0.3$. For the case $\delta/h = 0.45$, there is no inflection of $\langle T(z)\rangle$. The inflection of temperature profiles is characteristic of RBC, except that in RBC the

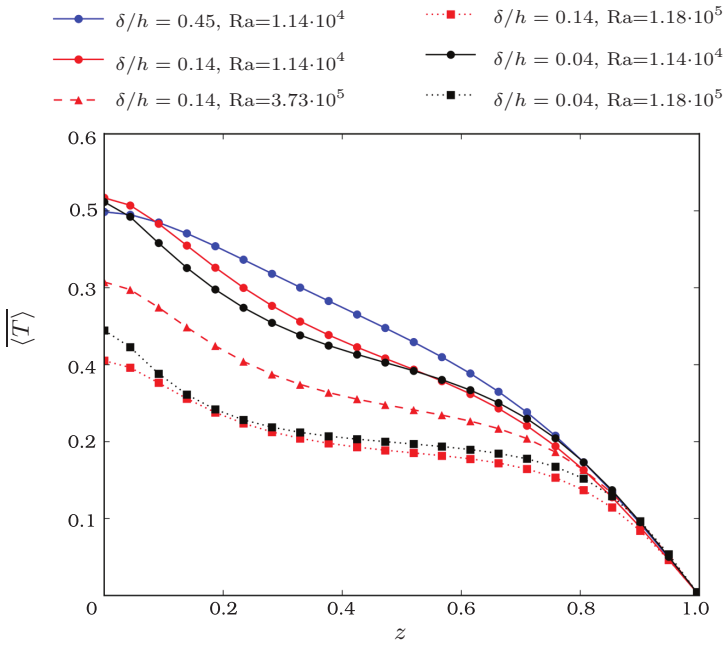

Fig. 6. Average temperature profiles.

profiles are symmetrical. On the top, the deposited energy fixes the outward heat flux on the top in the stationary regime. With the reference temperature chosen in Eq. (10), the non-dimensional heat flux on the top is simply $\partial T/\partial z = -1$, as seen in Fig. 6. In the case of internal heating, the characterization of global heat transfer differs from the RBC case, since there the heat flux is fixed. In the case of homogeneous internal heat sources, Goluskin and van der Poel [8] show that the non-dimensional mean fluid temperature is a good indicator of convective transfer and scales as

$$T_{\text{mean}} \sim \text{Ra}^{-1/5} \tag{12}$$

for homogeneous sources with

$$T_{\text{mean}} = \int_0^1 \langle T(z) \rangle \mathrm{d}z.$$

They confirmed this law for homogeneous heating with DNS. In the case of concentrated heating in the skin layer, this scaling is still valid, as seen in Fig. 7, which is a direct consequence of the low influence of δ/h on the temperature profiles (Fig. 6).

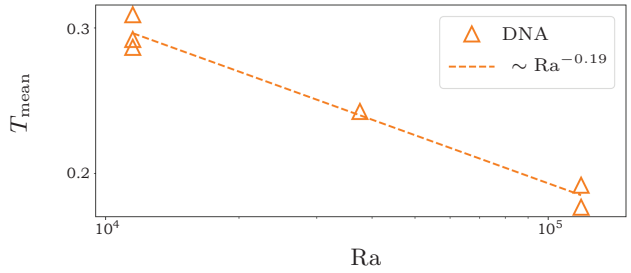

Fig. 7. T_{mean} vs. Ra. The dashed line is a linear fit of the data.

For a constant Ra, the points at different δ/h are superimposed. The weak effect of the skin depth is due to the sufficient mixing which homogenizes the flow by advecting heat.

3. Conclusions. In this paper, we analyzed using DNS the effects of the skin depth on the convection generated by induction heating for $\delta/h < 0.5$ and $10^4 <$ Ra $< 1.5 \times 10^5$. The features of classical RBC were observed in the AC field generated convection. In this range of parameters, the skin depth has a weak in-fluence and the heat repartition does not have influence on the flow. In particular, the skin depth influences very little the flow profiles (velocity and temperature) as well as the integrated quantities (mean kinetic energy and mean temperature). This is due to sufficient mixing because the computed points are far from the mar-ginal stability. At large magnetic Reynolds numbers, these conclusions are likely to change.

4. Acknowledgments. The present study is funded by the French Atomic Energy Commission (CEA) and by the ECM Company. The work was gran-ted access to high performance computing from Calmip (Project No. P0910) and Genci-Cines (Grant No. A0022B07400). The authors greatly acknowledge the help of Annaïg Pedrono for the numerical developments in the Jadim code.

References

[1] R. Moreau. *Magnetoohydrodynamics* (Springer, 1990).

[2] V.R. Gandhewar, V. Bansod and A. Borade. Induction furnace. A review. *International Journal of Engineering and Technology*, vol. 3 (2011), no. 14, pp. 277–284.

[3] J. Aurnou and P. Olson. Experiments on Rayleigh–Bénard convection, magnetoconvection and rotating magnetoconvection in liquid gallium. *Journal of Fluid Mechanics*, vol. 430 (2001), pp. 283–307.

[4] S. Renaudière de Vaux, R. Zamansky, W. Bergez, Ph. Tordjeman and J.F. Haquet. Magnetoconvection transient dynamics by numerical simulation. *The European Physical Journal E*, vol. 40 (2017), no. 40, 13.

[5] C. Journeau, P. Piluso, J. Haquet *et al.* Two-dimensional interaction of oxidic corium with concretes: The VULCANO VB test series. *Annals of Nuclear Energy*, vol. 36 (2009), no. 110, pp. 1597–1613.

[6] Y. Tasaka and Y. Takeda. Effects of heat source distribution on natural convection induced by internal heating. *International Journal of Heat and Mass Transfer*, vol. 48 (2005), no. 16, pp. 1164–1174.

[7] D. Goluskin. *Internally Heated Convection and Rayleigh-Bénard Convection.* (Springer, 2015).

[8] D. Goluskin and E. van der Poel. Penetrative internally heated convection in two and three dimensions. *Journal of Fluid Mechanics*, vol. 791 (2016), R6.

[9] J. Magnaudet, M. Rivero and J. Fabre. Accelerated flows past a rigid sphere or a spherical bubble. Part 1. Steady straining flow. *Journal of Fluid Mechanics*, vol. 284 (1995), pp. 97–135.